Nanomanufacturing and Metrology (2024) 7:8
https://doi.org/10.1007/s41871-024-00226-9

ORIGINAL ARTICLE

Influence of Film Thickness on Nanofabrication of Graphene Oxide

Chuan Tang[1] · Lei Chen[1] · Linmao Qian[1]

Received: 1 December 2023 / Revised: 20 February 2024 / Accepted: 26 February 2024
© The Author(s) 2024

Abstract

Nanofabrication of two-dimensional materials through mechanical machining is normally influenced by not only process parameters such as load and velocity but also intrinsic properties such as strength and thickness. Herein, we examined the effects of graphene oxide (GO) film thickness on nanofabrication on the plane surfaces and at the step edges using scanning probe microscope lithography. The material removal of GO initiates at the load above a critical value, which strongly depends on film thickness and locations. With the increase in film thickness, the critical load decreases monotonically on the plane surfaces but increases gradually at the step edges. Further, the critical load for the GO monolayer at the step edges is at least 25 times lower than that on the plane surfaces, and the gap decreases to around 3 times when GO thickness increases to four layers. Then, mechanical nanofabrication initiating from the GO step edge allows producing various nanopatterns under extremely low loads around 1 nN. Finally, the GO nanostructures are deoxidized by annealing at 800 °C in high-purity argon to restore their highly functionalized conjugated structures, which are supported by X-ray diffraction and Raman characterizations. This work provides a novel approach to fabricating graphene-like nanostructures by deoxidizing GO after nanofabrication, which holds significant potential for applications in graphene-based devices.

Graphical Abstract

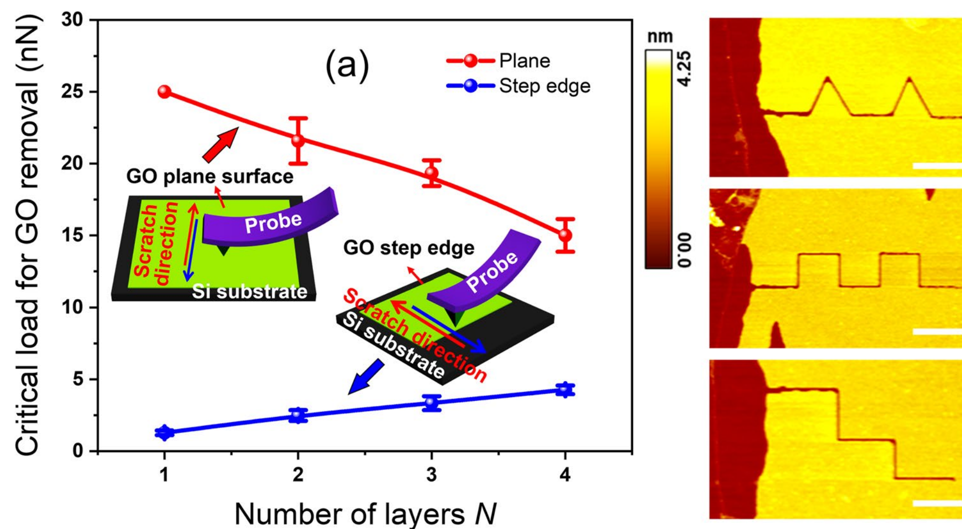

Extended author information available on the last page of the article

Published online: 03 April 2024

Highlights

1. The minimum load for GO removal initiation presents negative layer dependence on the plane surface but positive at the step edge.
2. The minimum load for GO monolayer nanofabrication at the step edge is at least 25 times lower than that at the plane surface.
3. GO nanopatterns can be fabricated under a low load and further deoxidized by high-temperature annealing.

Keywords Graphene oxide · Nanofabrication · Film thickness · step edge · Nanopattern · Deoxidized treatment

1 Introduction

Graphene, renowned for its remarkable optical, electrical, and mechanical properties, has been envisioned as a highly promising material with applications in various devices such as optoelectronic devices, sensors, field-effect transistors, and spintronic devices [1–4]. However, nanofabrication of these nanoelectronic devices that depend on various nanostructures is still extremely difficult due to the ultrahigh mechanical strength and chemical inertness of the graphene layer.

At present, several nanomanufacturing technologies have been developed for graphene, such as top-down electron-beam [5] or ion-beam [6, 7] lithography, laser ablation [8], plasma etching [9], scanning probe microscope (SPM) lithography [10], and bottom-up molecular self-assembly synthesis [11, 12], and they have their own advantages and disadvantages. For example, graphene patterns with different dimensions can be prepared through electron- and ion-beam etching [5–7]; however, the use of masks may cause incomplete removal of the resist residues after etching [13, 14] and adsorption of the charged electrons and particles [15], thereby negatively impacting the performance of the fabricated nanodevice. Meanwhile, although bottom-up molecular self-assembly provides controllable fabricated nanoribbons with different widths and edge atomic structures, its high costs and harsh preparation conditions of high temperatures and pressures limit large-scale mass production [11, 12].

More recently, SPM-based lithography, particularly scanning tunneling microscope (STM) lithography, has emerged as a promising approach for nanoscale patterning of graphene, offering simplicity and precise control over structure and location [10]. However, the tunneling current induced by the STM tip inevitably damages the electronic structure of graphene edges during nanomanufacturing, resulting in reduced device performance [16]. In addition, STM lithography is suitable in ultrahigh vacuum conditions, which is associated with complex operations and high costs. On this subject, atomic force microscope (AFM), as a type of SPM, has advantages over STM in nanomanufacturing due to its high efficiency, cost-effectiveness, and ambient environments. Moreover, AFM enables combining different approaches, such as chemical [17] and electrical [18] methods, to improve nanomanufacturing capabilities. While using hard probes for mechanical scratching has been applied for the fabrication of graphene nanostructures, this often causes partial peeling and uncontrollable damage to shape and size [19]. Electrochemical etching based on AFM can make graphene patterns depend on the electrochemical reaction between the electrically biased probe, graphene, and their interfacial meniscus [20]. However, this method causes oxidized pattern edges and bumpy structures at the contact zone with the probe [21, 22].

Preserving the structural integrity of graphene during fabrication is crucial to determine nanodevice performance. Minimizing damage to graphene and preserving its excellent properties are of great importance. Thus, developing a novel manufacturing method with lower processing environment requirements and a simple process is essential to obtain ordered edge structures. It is challenging to manufacture directly graphene on its plane due to its ultrahigh mechanical properties (high fracture strength, hardness, and fatigue strength), and even if possible, graphene nanostructures are destroyed. Meanwhile, graphene oxide (GO), as a graphene-based material, exhibits weaker mechanical properties than graphene, making it suitable for the flexible and controllable fabrication of various nanostructures [23, 24]. Through chemical reduction, high-temperature graphitization, electrochemical reduction, and solvent thermal reduction for deoxygenation, the electrical conductivity of GO can be improved [25]. Deoxidation treatment of GO for the production of graphene nanostructures is a well-known, attractive method due to its efficiency and cost-effectiveness. Although most studies have concentrated on various methods for the deoxidation treatment of GO, there is still a lack of research on the postfabrication deoxidation treatment of GO nanostructures. Moreover, nanofabrication parameters (such as cutting force and manufacturing time and speed) for graphene or other two-dimensional (2D) materials vary with different film thicknesses, and the effects of film thickness on material removal in nanofabrication still need to

be explored. Therefore, investigations of such the effects of film thickness and a simple, efficient approach involving the fabrication of graphene nanostructures by removing oxygen-containing GO functional groups after nanomanufacturing are crucial for various applications of graphene-based nanoelectronic devices.

Herein, a method of SPM lithography coupled with annealing was developed to fabricate nanopatterns of graphene-like materials based on the characterizations of load-dependent material removal at the atomic step edges and on the in-plane surfaces, and the effects of film thickness for material removal were examined. This work would help in the widespread applications of graphene-based materials, especially in micro/nanodevices.

2 Materials and Methods

2.1 Sample Preparation

GO was synthesized using the modified Hummer's method [26]. In this method, as raw material, graphite was oxidized by $KMnO_4$ and $NaNO_3$ in concentrated sulfuric acid, followed by annealing of the GO solution at 95 °C for 30 min. Subsequently, the GO nanoflakes were uniformly dispersed in deionized (DI) water by ultrasonication for 1 h. The GO suspension was deposited onto the silicon substrate covered with a ~ 0.8-nm-thick native oxide at the outermost surface [27]. The GO samples were heated and dried at 60℃ for 10 min to ensure effective adhesion and stable deposition of the GO layer onto the silicon substrate. Before deposition, the silicon substrate was meticulously cleaned through sonication in ethanol and DI water for 5 min, followed by drying under a stream of dry nitrogen to eliminate any contaminants and ensure a pristine substrate surface. The phase structure of the prepared GO was characterized using X-ray diffraction (XRD, Bruker D8 Advance, USA, Cu Kα source). Raman spectroscopy (LabRAM HR Evolution, Horiba, Japan) with a 532-nm wavelength was employed to analyze the structural features of GO nanosheets. The overall structure of the prepared GO was imaged using transmission electron microscope (TEM, JEM-2100 F, Japan) by dripping a GO suspension onto a copper grid. The thickness of the GO samples was determined using SPM (SPI3800N, Seiko, Japan).

2.2 Nanofabrication

During nanofabrication, reciprocating movements of the probe were executed across the in-plane surface or the step edge of GO using SPM in the contact mode under room conditions (temperature = 23 °C ± 2 °C, relative humidity = 45% ± 5%). The lateral forces in both forward and backward directions along the single line during probe sliding were simultaneously recorded simultaneously by the SPM software. Silicon nitride SPM probes (Si_3N_4, MLCT, Bruker, USA) with a precisely determined radius of 35 ± 7 nm (measured by SEM, JSM-7800 F, Japan) were employed, and their normal spring constant was calibrated to be ~ 0.1 N/m using Sader's method [28]. Throughout nanofabrication, the sliding length was maintained constant at 1 μm for plane surfaces and 2 μm for step edges, with a consistent sliding speed of 2 μm/s.

2.3 High-Temperature Annealing

To improve the electrical conductivity of the GO, the GO film was set into a horizontal tubular furnace (OTF-1200X-II, China) for high-temperature annealing treatment. The temperature within the furnace was gradually increased from room temperature to 800 °C at a heating rate of 5 °C/min while passing high-purity argon (99.99%) continuously at a rate of 80 mL/min. Upon reaching 800 °C, the film was maintained at this temperature for an additional duration of 2.0 h to facilitate further deoxidation. Finally, the tubular furnace was gradually cooled down to room temperature under the protective argon atmosphere.

3 Results and Discussion

3.1 Characterizations of the GO Nanosheets

Figure 1a and b show the topography and friction images of the prepared GO films obtained on the silicon substrate. The height of the GO film was measured to be ~ 1.82 nm by the Si_3N_4 probe (Fig. 1c), indicating a bilayer GO film (two times compared to the monolayer thickness of ~ 0.9 nm reported previously) [29]. The friction image and the cross-sectional profile show that the 2-layer GO nanosheets provide better friction reduction than the silicon substrate (Fig. 1d). The structural feature and surface topography of GO nanosheets were characterized by Raman spectroscopy and TEM, respectively. The Raman spectrum in Fig. 1e shows peaks at around 1350 cm^{-1}, which is assigned to the D band (corresponding to lattice disorders, vacancies, and defects in materials), and around 1580 cm^{-1}, which corresponds to the G band (arising from in-plane stretching vibrations of carbon–carbon bonds in a hexagonal lattice) [26, 30, 31], which are structure characteristics of GO. However, the 2D band (associated with the second-order double-resonance process involving two phonons) at 2700 cm^{-1} vanishes due to high oxidation. In the TEM image in the inset of Fig. 1e,

GO nanosheets contain lamellar structures and numerous surface wrinkles, further indicating the presence of disorder and defects [32, 33]. The XRD pattern in Fig. 1f shows the complete disappearance of the graphitic peak at 26.3° (002) and the observation of a new broad diffraction peak at $2\theta = 11.4°$ (001), which indicates an interlayer distance of ~ 0.78 nm for the GO [30]. After complete oxidation, numerous oxygen-containing functional groups and defects are formed on the surface, resulting in a slightly larger thickness of monolayer GO (~ 0.9 nm) than the measured lattice spacing of ~0.78 nm estimated from the XRD spectrum due to the adsorption of water molecules from the atmosphere [34, 35].

3.2 Material Removal on the GO Plane Surface and at the Step Edge

Previous studies have shown that material removal on the in-plane surface of a mechanically exfoliated monolayer graphene cannot happen at the relatively low mechanical loads, and structural destruction of both graphene and the underlying substrate may occur under the extremely high contact stresses [36–38]. Although nanostructures can be fabricated at the graphene edge step at the low load conditions, the fabricated graphene edges become substantially rough or suffer uncontrolled detachment from the substrate [19, 38, 39]. The mechanical properties of graphene are greatly reduced after oxidation, rendering it more suitable for nanomanufacturing, which provides opportunities for more nanostructured devices [23, 24, 40]. In this study, nanofabrication on both the monolayer plane surface and step edge of GO samples was performed using the Si_3N_4 probes (radius = 35 ± 7 nm) at room temperature (Fig. 2a and d). After 200 reciprocating sliding cycles at a maximum load of 25 nN, the GO monolayer (thickness: ~0.91 nm, inset of Fig. 2b) exhibited no discernible damage, as well as no considerable changes in the magnitude of the lateral force signal (Fig. 2c). The GO monolayer exhibited an excellent resistance to damage, which hold intact even after more than 200 cycles. Conversely, at the step edge, the monolayer GO (~ 0.92 nm, inset of Fig. 2e) was destroyed after 20 cycles with an applied load of only 1 nN (Fig. 2e). Once GO damage was initiated at the step edge, the friction force signal of the GO region exhibited a considerable increase and gradually further increased with increasing number of cycles (Fig. 2f). The GO was destroyed starting from the second sliding cycle and was completely removed within six cycles. Clearly, the GO plane surface demonstrated excellent resistance to damage, whereas the step edge is vulnerable to wear, and its minimum load required for material removal of the GO layer can be substantially reduced. This susceptibility should be attributed to the numerous original defects at the step edge.

3.3 Layer-Dependent Material Removal of GO Nanosheets

Further examination of the nanofabrication of the GO layer on the plane surface and at the step edge was conducted by determining the required load of nanofabrication depending on GO thickness. The in-plane nanofabrication results of GO with 1–4 layers under applied loads of 5–25 nN are shown in Fig. 3a–d. For monolayer GO (thickness: ~0.91 nm, upper inset in Fig. 3a), no surface damage was observed on the internal plane for all load conditions after 20 reciprocating sliding cycles (Fig. 3a). Moreover, there was no substantial change in the cross-sectional profile (Fig. 3e), which further confirmed that even at 25 nN, damaging the monolayer GO was difficult. However, after 20 cycles above 20 nN, the bilayer GO (thickness: ~1.82 nm, inset profile in Fig. 3b) was destroyed (Fig. 3b).After increasing the number of layers to 3 and 4 (thicknesses: ~2.74 and ~ 3.65 nm, inset profiles in Fig. 3c and d, respectively) the GO were destroyed after 20 cycles under an low applied load of 15 nN. These results show that the critical load to initiate material removal in nanofabrication on the plane surface decreases from above 25 nN (maximum load applied by the Si_3N_4 probe) to 15 nN with increasing thickness from one to four layers. Furthermore, the cross-sectional profiles of the damage scars measured at the fabrication locations agreed with the height profiles of the GO layers, indicating that the GO layers inside the sliding regions were completely removed (Fig. 3f–h). Interestingly, the critical load of nanofabrication is larger for thinner GO layers. This indicates that with increasing GO thickness, the nanofabrication load of GO on the substrate decreases gradually (from one to four layers), which agrees with previous research on GO and other 2D materials (such as fluorinated graphene and $NbSe_2$) [29, 41, 42].

For comparison, Fig. 3i–l present the topographies of GO with 1–4 layers after nanofabrication at the step edge with applied loads of 1–5 nN. At the monolayer GO step edge, material removal can occur even with an applied load as low as 1 nN (Fig. 3i). As the number of GO layers increases, the critical load required for step-edge nanofabrication increases. The critical (minimum) load for nanofabrication at the step edge increases from 1 nN for the monolayer to 5 nN for four layers (Fig. 3j–l). The cross-sectional profile heights of the nanofabricated scars match the thickness of the corresponding GO layers (insets of Fig. 3i–l and m–p). GO is a layered 2D material, which is either removed layer-by-layer or completely removed during nanofabrication. The fact that the removal depth of GO on the substrate is consistent with its film thickness strongly supports the complete removal of the GO layer from the substrate. This observed thickness dependence in the nanofabrication of the GO step edge is exactly the same as the nanofabrication observed in

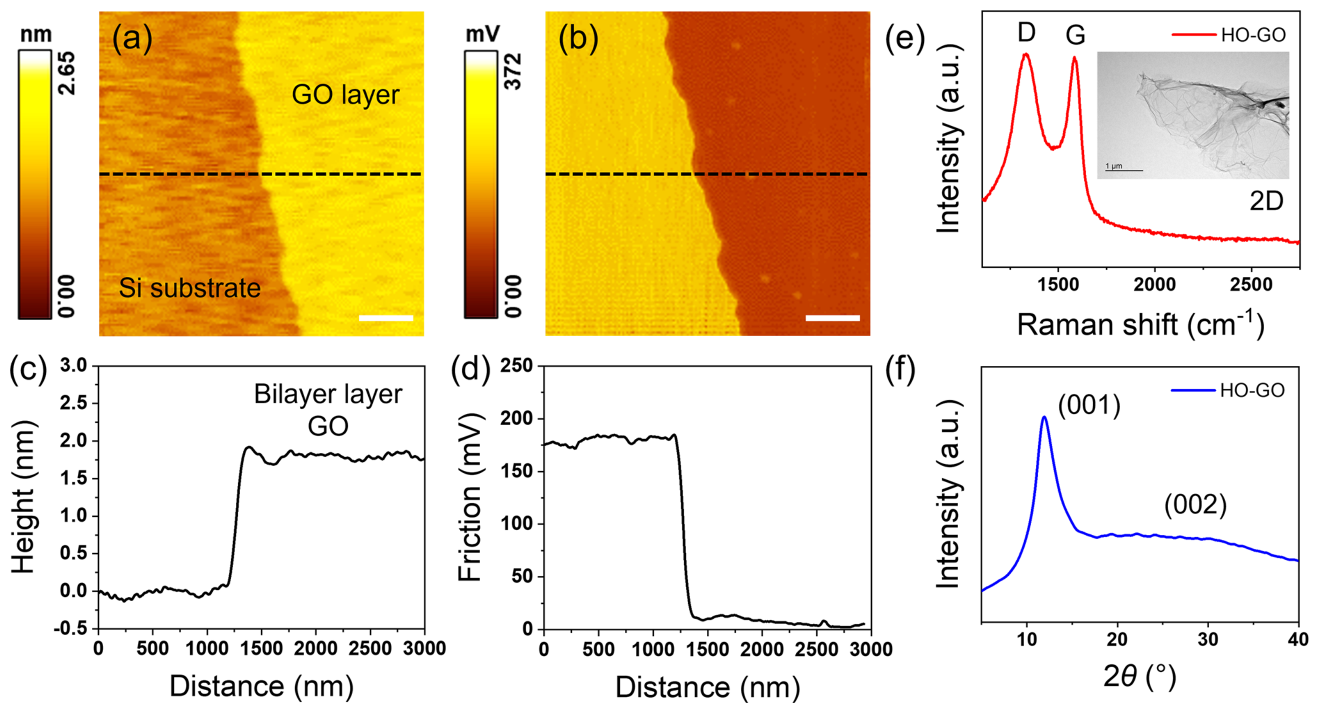

Fig. 1 Characterization of the GO nanosheets. SPM topography **a** and corresponding friction image **b** of bilayer GO on silicon. The scale bar is 0.5 μm. Cross-sectional profile of height **c** and friction force **d** of bilayer GO measured along the black dotted lines in the topography and friction images, respectively. Raman **e** and XRD spectra **f** of GO. The inset in **e** shows the TEM image of the GO nanosheets

mechanically exfoliated graphene, MoS_2, h-BN, and other 2D layered materials, highlighting that thicker layers pose more challenges during fabrication [43].

As indicated in prior research, the critical load for material removal on the plane surface of GO deposited on a native silicon oxide substrate demonstrates a decreasing trend with increasing film thickness, which corresponds to the underlying wear mode of the overall removal [29]. Density function theory calculations revealed that the overall removal of GO is dominated by adhesive strengths between the substrate and GO, which is correlated with GO thickness originating from differences in interfacial charge transfer. Meanwhile, the critical loads of nanofabrication initiation at the GO step edge are reverse, i.e., the critical load for nanofabrication monotonically increases with increasing number of layers (Fig. 4). Similarly, the GO nanofabrication at the step edge is also an overall removal. These results show that the adhesive strength of the substrate has a relatively minor impact on nanofabrication at the step edge, which may be due to direct contact between the probe and both the substrate and GO step edge during reciprocating sliding. Given the relative homogeneity of GO films, the direct positive correlation between the required critical loads for nanofabrication and the GO thickness can be attributed to the bending stiffness of the GO layer. Moreover, the natural defects on the step edges of GO nanosheets greatly reduce the performance of the GO layers, allowing nanofabrication to proceed at the lower loads. Compared to nanofabrication on the GO plane surface, the critical loads for nanofabrication of the GO step edge were reduced by at least 25 times to 3 times from monolayer to four layers (Fig. 4).

3.4 Evolution of Material Removal for the GO Nanosheets

The critical (minimum) loads for GO removal on the plane surfaces and at the step edges exhibit a pronounced dependence on the number of layers. Additionally, the GO film thickness dependence on nanofabrication depends on the number of sliding cycles. To determine the effects of sliding cycles for GO nanofabrication on the plane surface and at the step edge, Fig. 5 compares the evolution of nanofabrication for different sliding cycles of monolayer (thickness: ~0.91 nm) and four layers (thickness: ~3.72 nm) GO. For nanofabrication at the GO step edge under 1 nN, complete removal of the monolayer GO at the step edge after six cycles was observed (Fig. 5a and b), while that of the four-layer GO inside the sliding region was observed until 45 sliding cycles (Fig. 5c and d), clearly showing an enhanced resistance to removal of thicker films.

For nanofabrication inside the GO plane, under 25 nN, the material removal of the monolayer GO plane was initiated at the ~645th cycle (Fig. 5e and f) and was completely

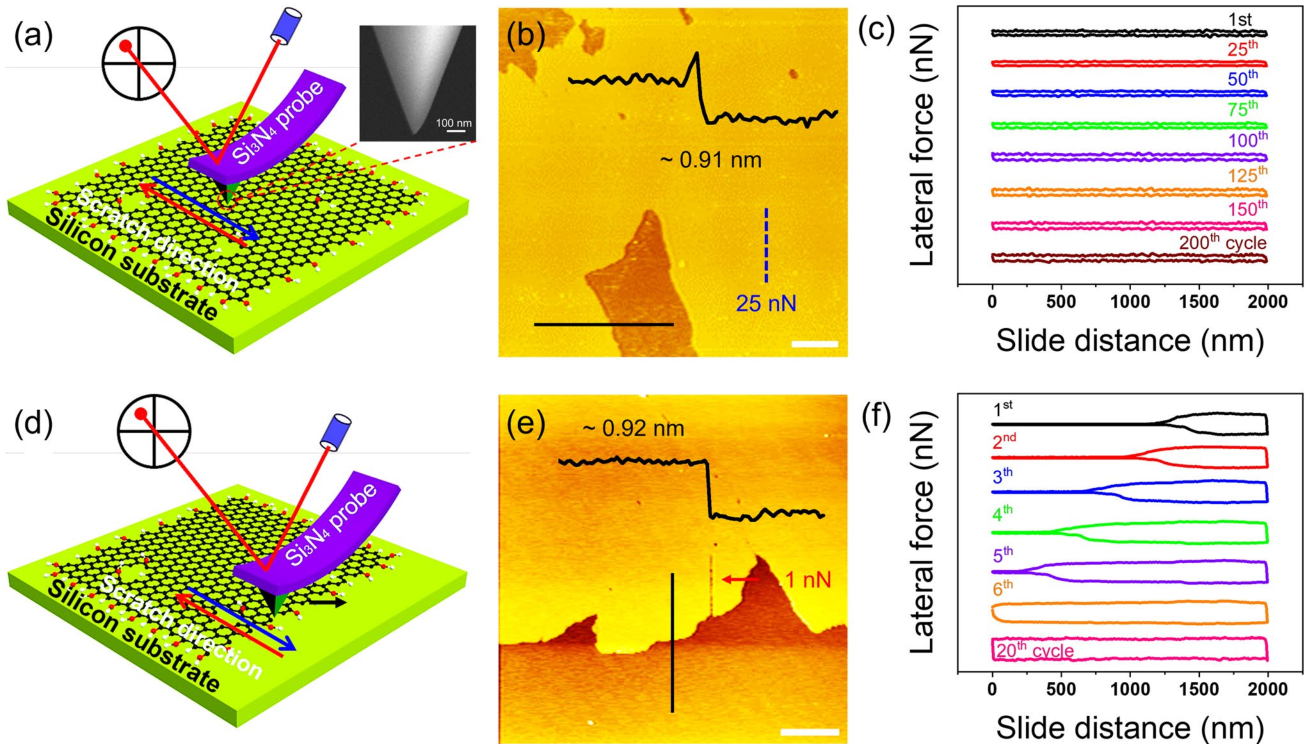

Fig. 2 Material removal of the GO monolayer on the plane surface and at the step edge. Schematic of the nanofabrication experiment performed on the GO plane surface **a** and at the step edge **d** using the Si_3N_4 probe. Nanofabrication morphologies of the GO monolayer on the plane surface **b** and at the step edge **e**. Lateral force–distance curves recorded at the different reciprocating cycles on the plane surface **c** and at the step edge **f**. The insets in **b** and **e** show the cross-sectional profiles of monolayer GO. Scale bars are 1 μm in **b** and **e**

removed at the ~750th cycle, while that for a four-layer GO on the plane surface was initiated from the ~13th sliding cycle and ended at the 18th cycle (Fig. 5g and h). The matched values between the wear depth (bottom inset in Fig. 5g) and the GO thickness indicate that the GO layers are completely worn out. Similar to the load requirements of thickness-dependent manufacturing (Fig. 3), the nanofabrication of the monolayer GO film is more difficult to be processed than multilayer films, that is, more manufacturing cycles are required under a given load.

Figure 6 further compares the averaged critical sliding cycles (minimum number of sliding cycles to induce material removal) for GO nanofabrication of the monolayer plane, multilayer plane, monolayer step, and multilayer step at normal loads of 1 nN for the step edge and 25 nN for the internal plane. For the material removal of monolayer films in the interior plane, most of the critical cycles are larger than 1000, while fewer parts of the critical cycles are lower than 800, resulting in an average value of approximately 830 times for material removal.

In comparison, the averaged critical cycle for the four-layer plane decreased dramatically down to 11 times (Fig. 6a). For nanofabrication at the step edge, the averaged critical cycle for material removal at the monolayer step edges is 4, while that at the four-layer step edges increased to 36 (Fig. 6b). In general, the critical sliding cycles for GO removal followed the same trend as the critical load: monolayer step < multilayer step and multilayer plane < monolayer plane.

3.5 Removal Mechanism of GO Plane Surfaces and Step Edges

Previous research of GO on silica substrate revealed that broad oxygen-containing functional groups on GO lead to a stronger interaction with the substrate, resulting in the absence of the puckering effect and, thus, no friction dependence on thickness [44]. Moreover, it was demonstrated that the high adhesion between the graphene and the mica substrate results in no thickness dependence for friction [45]. In this study, the silicon substrate, with a native oxide outermost layer, is partially terminated by –OH groups [27], inducing high surface energy and promoting the formation of hydrogen-bond networks with the attached GO (inset of Fig. 7a) [46, 47]. This boosts in-plane stiffness, reducing the folding effect and enhancing damage resistance, particularly in direct contact with silicon (monolayer GO plane, Fig. 7a). Thus, substrate adhesion plays a dominant

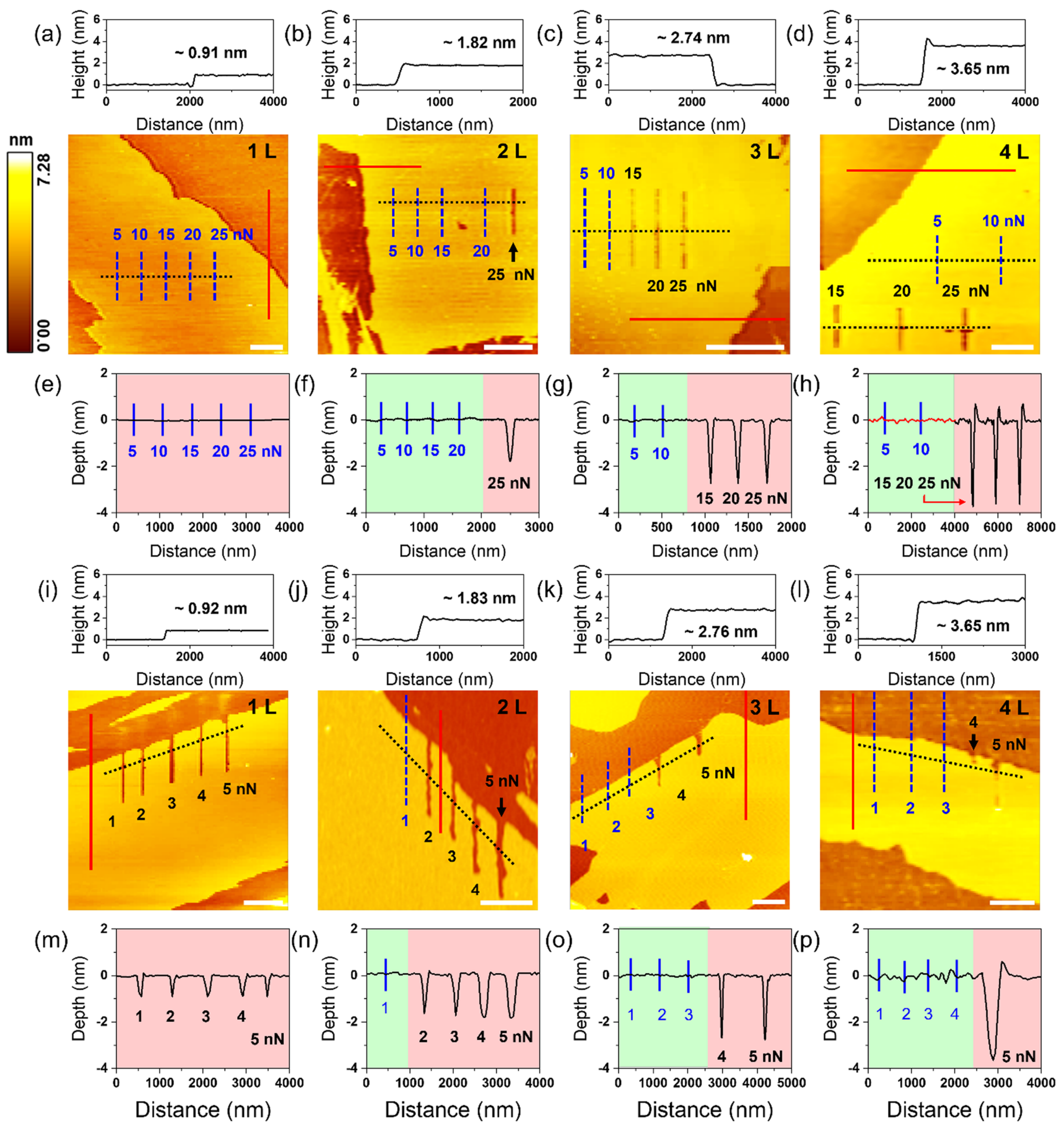

Fig. 3 Material removal of GO with different thicknesses at the step edges and inside the plane surfaces. **a–d** and **i–l** show the topographies and corresponding cross-sectional profiles of GO with different thicknesses after nanofabrication on plane surfaces under the applied loads of 5–25 nN and at the step edge under the applied loads of 1–5 nN, respectively. The upper insets of **a–d** and **i–l** show the cross-sectional profiles of mono-, bi-, three-, and four-layer (1 L, 2 L, 3 L, 4 L) GO, respectively. The scale bars are 1 μm. **e–h** and **m–p** show the cross-sectional profiles of the sliding regions on the plane surfaces and at the step edges (marked by the black dotted lines in the topographical images), respectively. The number of sliding cycles is kept constant at 20

role in plane nanofabrication. With GO thickness of up to four layers, the influence of adhesion strength originating from the silicon substrate surface on the thickness of the GO layer should be largely weakened, then resulting in an increase in wrinkling effects and a decrease in damage resistance (Fig. 7b); therefore, the nanofabrication load and sliding cycles of GO demonstrate a decreasing tendency with increasing thickness.

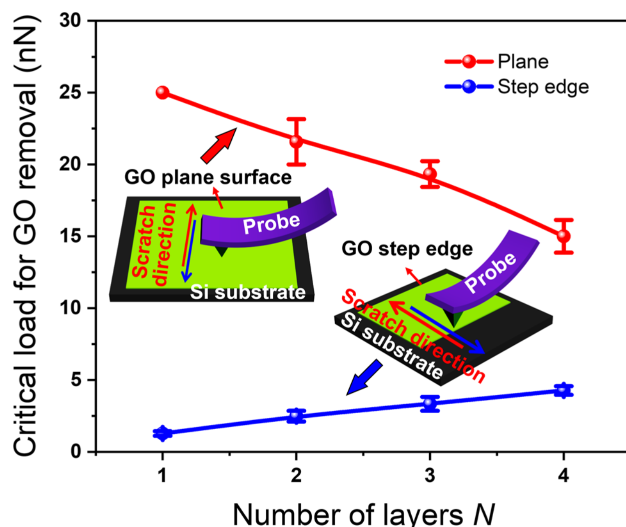

Fig. 4 Critical loads for material removal initiation at the step edge and on the plane surface as a function of the number of GO layers

Different from the plane surface, the integral strength of the GO step edge gradually improves with an increasing number of layers due to the cumulative effect of multilayer film thickness. The thicker GO layer is stiffer and has a higher ability to resist damage. The integral strength of the GO layer plays a dominant role in the nanofabrication of GO step edges instead of interfacial adhesion. Therefore, the critical load or cycle for nanofabrication initiated at the step edge is directly associated with layer thickness (Fig. 7c and d). The critical sliding cycles and loads for nanofabrication initiation at the step edge of monolayer GO films are the lowest compared with the multilayer film step, monolayer, and multilayer film plane. Thus, when employing nanofabrication initiated from the step edge, various GO nanostructures are easily obtained under lower loads.

3.6 Fabrication and High-Temperature Annealing of the GO Nanostructures

GO step edge is exceptionally weak and susceptible to damage at a low load of ~ 1 nN. Thus, manufacturing various GO nanostructures is more suitable for initiating from the edge under lower loads. In addition, the GO nanostructures were fabricated by the Si_3N_4 probe, where no damage debris was produced, and the edge structure remained intact, which is much different from the cases of graphene where considerable damage debris or contamination residues on the surface were often left after the mechanically fabricating, thus compromising the performance of graphene-based nanodevices. Using the developed method, various GO nanopatterns,

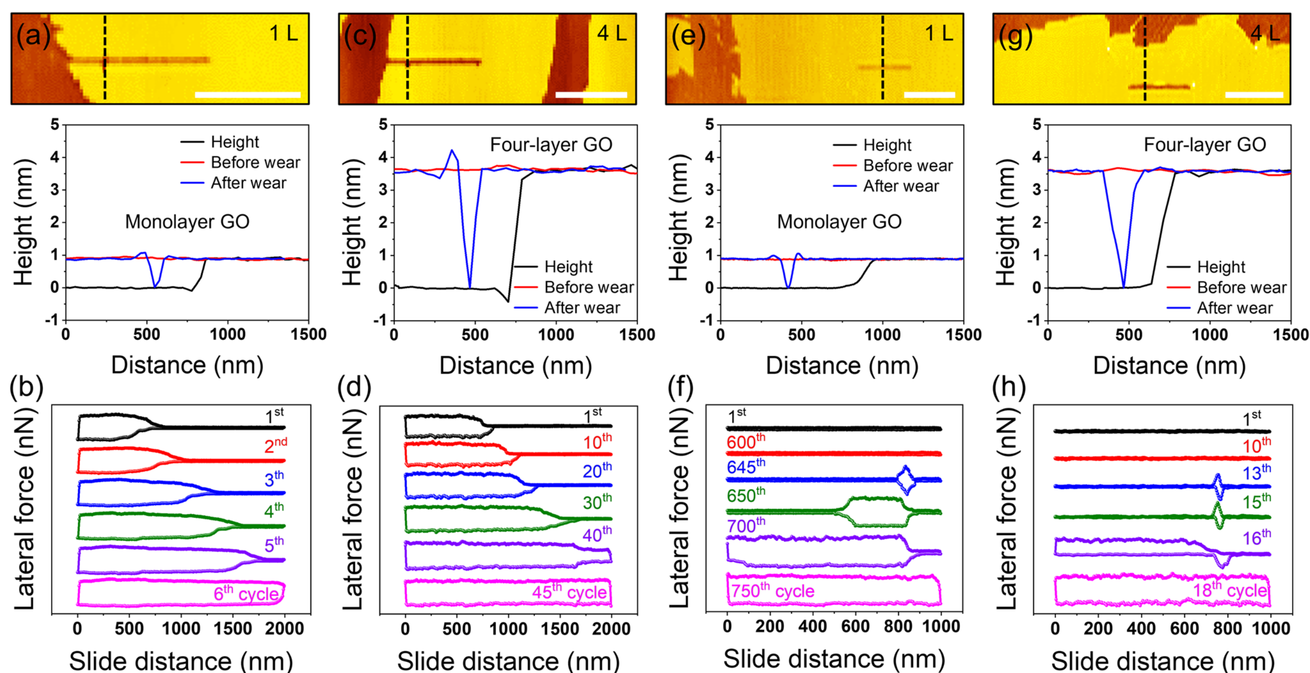

Fig. 5 Comparison of material removal and lateral force at the step edge and on the plane surface for nanofabrication of monolayer (1 L) and four-layer (4 L) GO nanosheets. Topographies and corresponding cross-sectional profiles (marked by the black dotted lines in the topographical images) of the GO monolayer step **a**, four-layer step **c**, monolayer plane **e**, and four-layer plane **g** after different sliding cycles. The scale bars are 1 µm. Lateral force–distance curves of the GO monolayer step **b**, four-layer step **d**, monolayer plane **f**, and four-layer plane **h** recorded at the different reciprocating cycles. Normal loads of 1 and 25 nN were applied at the step edges and on the plane surfaces, respectively

including triangular wave nanochannels, square wave nanochannels, step nanochannels, and nanochannel arrays, can be readily fabricated (Fig. 8a–d). Furthermore, the resulting GO nanopatterns can be further deoxygenated by high-temperature annealing, yielding nanostructures with similar electrical properties to graphene.

To improve the electrical conductivity and mechanical properties of the GO, annealing was applied to the nanochannel array in a horizontal tubular furnace at 800 °C. The height profile reveals a decrease in thickness of the deoxygenated GO layer from ~1.82 (bit layer, Fig. 8d and f) to ~1.12 nm (Fig. 8e and g) after annealing, indicating that the interlayer spacing of the deoxygenated GO monolayer reduced from ~0.91 to 0.56 nm, slightly higher than the thickness of graphene monolayer (~0.34 nm), which should be ascribed to the removal of most of the oxygen-containing groups intercalated between the graphene interlayers. XRD and Raman analyses were applied to further characterize the structural evolution after annealing. The XRD spectrum exhibited a shift in the diffraction peak position from $2\theta = 11.4°$ (001) to a higher angle of $2\theta = 25.6°$ (002) at 800 °C, indicating a considerable reduction in the lattice spacing from ~0.78 to ~0.35 nm (Figs. 1f and 8i), which can be associated with the gradual removal of interlayer species such as physically adsorbed water and most oxygen-containing functionalities during annealing. Due to the removal of unstable oxygen-containing groups during annealing, the interlayer spacing narrows and ultimately reaches the same spacing as graphite. However, the calculated interlayer spacing (~0.56 nm; Fig. 8g) of the deoxygenated GO is slightly higher than the theoretical value (~0.35 nm) estimated from the XRD spectrum, probably corresponding to the roughness of the substrate surface and the influence of a minor fraction of incompletely removed functional groups (such as epoxy group, etc.).

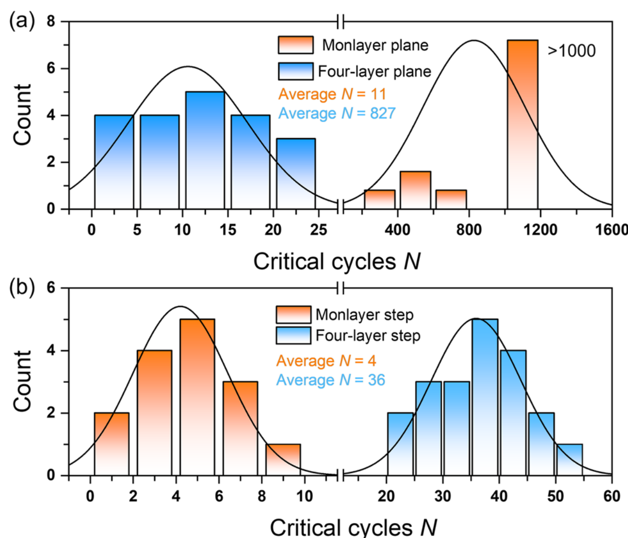

Fig. 6 Averaged critical cycles N of material removal initiation for nanofabrication of monolayer and four-layer GO. **a** Critical cycles for nanofabrication on the monolayer and four-layer GO plane surfaces. **b** Critical cycles for nanofabrication at monolayer and four-layer GO step edges. Normal loads of 1 and 25 nN were applied at the step edges and the plane surfaces, respectively

Furthermore, the Raman spectrum displays the D band around 1332 cm^{-1}, G band around 1588 cm^{-1}, and weak 2D band at 2700 cm^{-1}, which is associated with the second-order double-resonance process involving two phonons (Fig. 8h). Both the D and G peaks exhibited increased intensities and sharpened profiles, demonstrating structural changes of GO, which is further confirmed by the successful deoxygenation of GO by annealing at 800 °C. After annealing, the D band shifted from 1336 to 1332 cm^{-1} (Figs. 1e and 8h), and the intensity ratio of the D to G band increased from 1.02 to 1.15. The loss of oxygen-containing functionalities from the GO plane can lead to the formation of numerous structural defects, such as vacancies and distortions, thereby increasing the intensity ratio of the D to G band in the deoxygenated GO [48], which agrees with

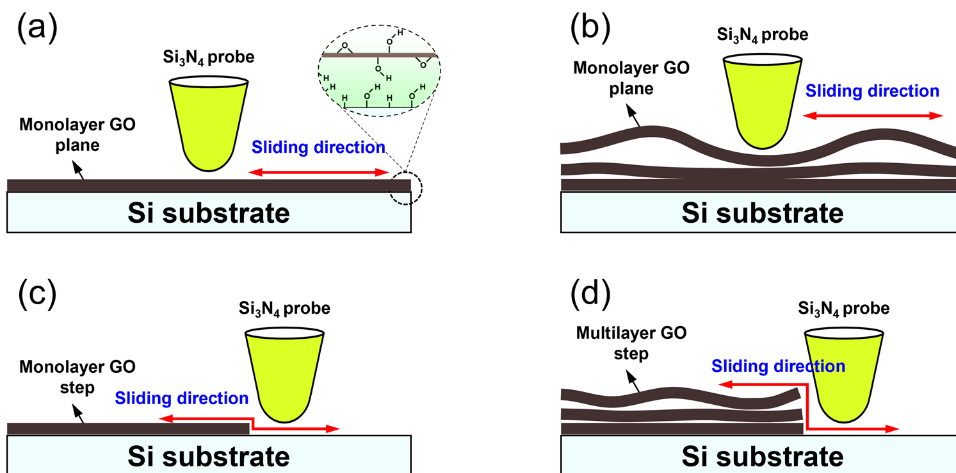

Fig. 7 Schematic of nanofabrication mechanisms of GO step edges and plane surfaces depending on thickness. Nanofabrication on monolayer **a** and multilayer **b** GO plane surfaces by reciprocating sliding of probes. The inset in **a** shows the silicon substrate with a native oxide outermost layer partially terminated by the –OH groups to form hydrogen-bond networks with the attached GO nanosheets [29]. Schematic of the sliding of a probe over monolayer **c** and multilayer **d** GO step edges

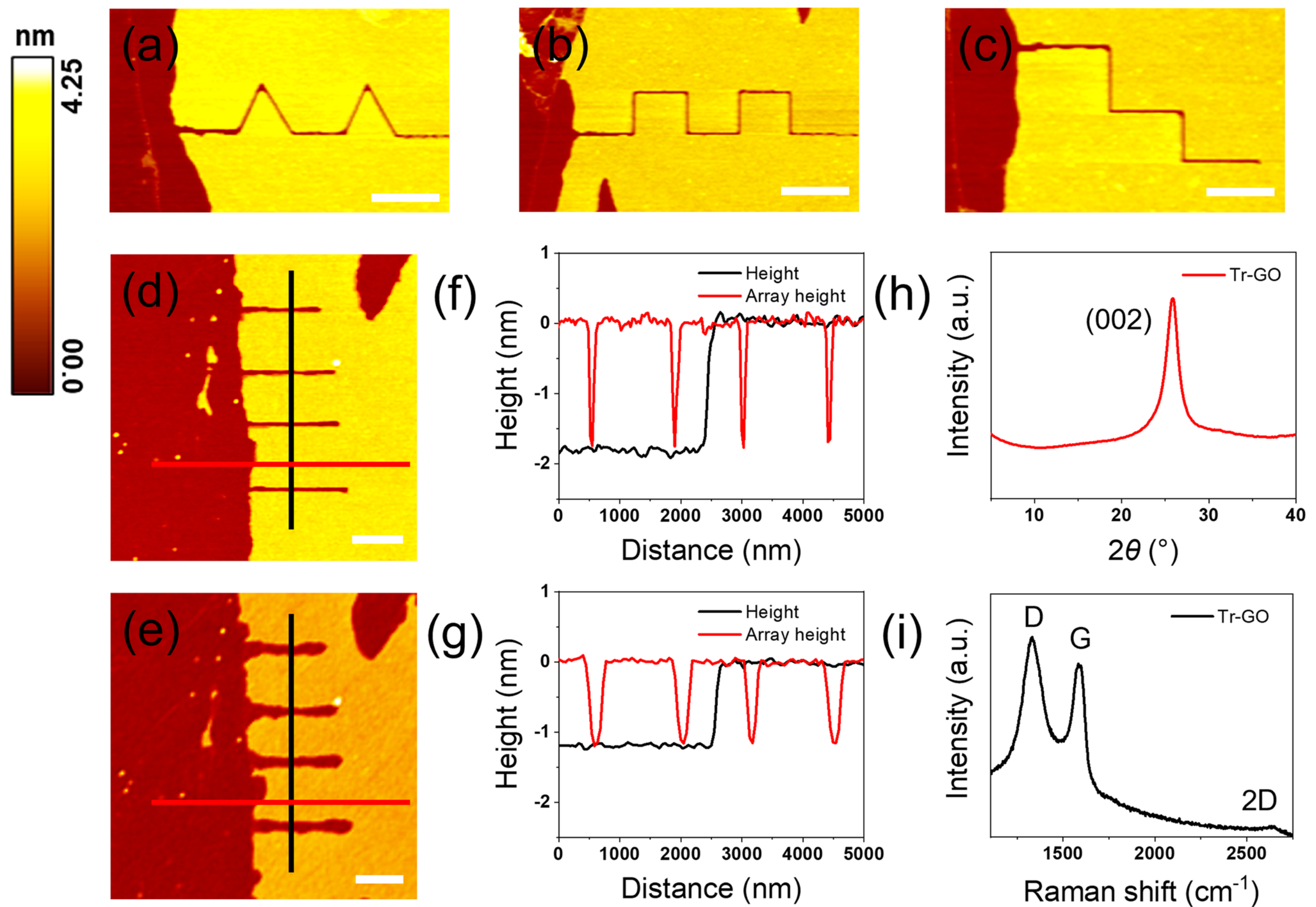

Fig. 8 Nanostructures fabricated on the GO layer in ambient air. Nanochannels fabricated: **a** triangular wave nanochannel, **b** square wave nanochannel, **c** step nanochannel, **d** nanochannel array before and **e** after high-temperature annealing. **f, g** Height profiles of the GO nanochannel array measured before and after high-temperature annealing. **h, i** Raman and XRD spectra of GO after high-temperature annealing. The scale bars are 1 μm in (**a**–**e**)

the deoxygenation treatment of GO by hydrazine hydrate, $NaBH_4$, or HI solution as reported elsewhere [49–51]. Based on this method, various nanopatterns with similar electrical properties to graphene can be fabricated to hold promise in graphene-based micro/nanodevices and sensors and gas detection systems based on a wide range of nanostructures [52–55].

4 Conclusions

Herein, the material removal of GO on the plane surface and at the step edge strongly depends on GO layer thickness. For nanofabrication on the GO plane surface, the nanofabrication loads or cycles of GO demonstrate an inverse layer dependence, i.e., the lesser the layer thickness, the larger the values for material removal initiation needed. Meanwhile, the critical loads or cycles of nanofabrication initiated at the step edge are directly associated with layer thickness. In general, the lowest critical cycle and load are needed for nanofabrication at the step edge of the GO monolayer, and thus, a method of SPM lithography for fabricating various GO nanopatterns, such as triangular waves, square wave nanochannels, step nanochannels, and nanochannel arrays, based on material removal initiated from the step edge under extremely low mechanical stress is developed. The fabrication of the deoxygenated GO nanostructures with intact edge structures by high-temperature annealing is achieved. In conclusion, this work presents a reliable, simple, flexible, and highly promising method for nanofabricating graphene-based electronic devices and sensors.

Acknowledgements This work was supported by the National Natural Science Foundation of China (Nos. 52350411, 52122507 and 52235004), Sichuan Science and Technology Program (2023NSFSC1988 and 2023YFSY0004), and the Fundamental Research Funds for the Central University (No. 2682021ZTPY095). The authors express their gratitude to the Analysis and Testing Center of Southwest Jiaotong University for their assistance in conducting the characterizations and experiments: SEM analyses of probes, TEM and Raman spectroscopy analyses of samples, and AFM tests.

Author Contributions All authors read and approved the final manuscript.

Availability of Data and Materials The authors declare that all data supporting the findings of this study are available within the article.

Declarations

Conflict of interest The authors declare that they have no conflicts of interest.

Open Access This article is licensed under a Creative Commons Attribution 4.0 International License, which permits use, sharing, adaptation, distribution and reproduction in any medium or format, as long as you give appropriate credit to the original author(s) and the source, provide a link to the Creative Commons licence, and indicate if changes were made. The images or other third party material in this article are included in the article's Creative Commons licence, unless indicated otherwise in a credit line to the material. If material is not included in the article's Creative Commons licence and your intended use is not permitted by statutory regulation or exceeds the permitted use, you will need to obtain permission directly from the copyright holder. To view a copy of this licence, visit http://creativecommons.org/licenses/by/4.0/.

References

1. Li X, Tao L, Chen Z, Fang H, Li X, Wang X, Xu J-B, Zhu H (2017) Graphene and related two-dimensional materials: structure-property relationships for electronics and optoelectronics. Appl Phys Rev 4:021306
2. Choi JH, Lee J, Byeon M, Hong TE, Park H, Lee CY (2020) Graphene-based gas sensors with high sensitivity and minimal sensor-to-sensor variation. ACS Appl Nano Mater 3:2257–2265
3. Fu W, Jiang L, Van Geest EP, Lima LMC, Schneider GF (2017) Sensing at the surface of graphene field-effect transistors sensing at the surface of graphene field-effect transistors. Adv Mater 29:1603610
4. Gregersen SS, Power SR, Jauho A-P (2017) Nanostructured graphene for spintronics. Phys Rev B 95:121406
5. Liu L, Tian S, Long Y, Li W, Yang H, Li J, Gu C (2014) Tunable periodic graphene antidot lattices fabricated by e-beam lithography and oxygen ion etching. Vacuum 105:21–25
6. Lemme MC, Bell DC, Williams JR, Stern LA, Baugher BW, Jarillo-Herrero P, Marcus CM (2009) Etching of graphene devices with a Helium ion beam. ACS Nano 3:2674–2676
7. Abbas AN, Liu G, Liu B, Zhang L, Liu H, Ohlberg D, Wu W, Zhou C (2014) Patterning, characterization, and chemical sensing applications of graphene nanoribbon arrays down to 5 nm using Helium ion beam lithography. ACS Nano 8:1538–1546
8. Sahin R, Simsek E, Akturk S (2014) Nanoscale patterning of graphene through femtosecond laser ablation. Appl Phys Lett 104:053118
9. Wang X, Dai H (2010) Etching and narrowing of graphene from the edges. Nat Chem 2:661–665
10. Garcia R, Knoll AW, Riedo E (2014) Advanced scanning probe lithography. Nat Nanotechnol 9:577–587
11. Cai J, Ruffieux P, Jaafar R, Bieri M, Braun T, Blankenburg S, Muoth M, Seitsonen AP, Saleh M, Feng X, Mullen K, Fasel R (2010) Atomically precise bottom-up fabrication of graphene nanoribbons. Nature 466:470–473
12. Llinas JP, Fairbrother A, Borin Barin G, Shi W, Lee K, Wu S, Yong Choi B, Braganza R, Lear J, Kau N, Choi W, Chen C, Pedramrazi Z, Dumslaff T, Narita A, Feng X, Mullen K, Fischer F, Zettl A, Ruffieux P, Yablonovitch E, Crommie M, Fasel R, Bokor J (2017) Short-channel field-effect transistors with 9-atom and 13-atom wide graphene nanoribbons. Nat Commun 8:633
13. Park D-H, Cho YJ, Lee J-H, Choi I, Jhang SH, Chung H-J (2019) The evolution of surface cleanness and electronic properties of graphene field-effect transistors during mechanical cleaning with atomic force microscopy. Nanotechnology 30:394003
14. Jo I, Pettes MT, Kim J, Watanabe K, Taniguchi T, Yao Z, Shi L (2013) Thermal conductivity and phonon transport in suspended few-layer hexagonal boron nitride. Nano Lett 13:550–554
15. Stanford MG, Pudasaini PR, Cross N, Mahady K, Hoffman AN, Mandrus DG, Duscher G, Chisholm MF, Rack PD (2017) Tungsten diselenide patterning and nanoribbon formation by gas-assisted focused-Helium-ion-beam-induced etching. Small Methods 1:1600060
16. Tapaszto L, Dobrik G, Lambin P, Biro LP (2008) Tailoring the atomic structure of graphene nanoribbons by scanning tunnelling microscope lithography. Nat Nanotechnol 3:397–401
17. Dazzi A, Prater CB (2017) AFM-IR: technology and applications in nanoscale infrared spectroscopy and chemical imaging. Chem Rev 117:5146–5173
18. Zhang S, Gao L, Song A, Zheng X, Yao Q, Ma T, Di Z, Feng XQ, Li Q (2018) Tuning local electrical conductivity via fine atomic scale structures of two-dimensional interfaces. Nano Lett 18:6030–6036
19. Vasić B, Matković A, Gajić R, Stanković I (2016) Wear properties of graphene edges probed by atomic force microscopy based lateral manipulation. Carbon 107:723–732
20. Han W, Mathew PT, Kolagatla S, Rodriguez BJ, Fang F (2022) Toward single-atomic-layer lithography on highly oriented pyrolytic graphite surfaces using AFM-based electrochemical etching. Nanomanuf Metrol 5:32–38
21. Ahn JJ, Jo YD, Kim SC, Lee JH, Koo SM (2011) Crystallographic plane-orientation dependent atomic force microscopy-based local oxidation of silicon carbide. Nanoscale Res Lett 6:1–5
22. Jiang Y, Guo WL (2008) Convex and concave nanodots and lines induced on HOPG surfaces by AFM voltages in ambient air. Nanotechnology 19:345302
23. Lu G, Zhou X, Li H, Yin Z, Li B, Huang L, Boey F, Zhang H (2010) Nanolithography of single-layer graphene oxide films by atomic force microscopy. Langmuir 26:6164–6166
24. He Y, Dong H, Li T, Wang C, Shao W, Zhang Y, Jiang L, Hu W (2010) Graphene and graphene oxide nanogap electrodes fabricated by atomic force microscopy nanolithography. Appl Phys Lett 97:133301
25. Zhang K, Fu Q, Pan N, Yu X, Liu J, Luo Y, Wang X, Yang J, Hou J (2012) Direct writing of electronic devices on graphene oxide by catalytic scanning probe lithography. Nat Commun 3:1194
26. Marcano DC, Kosynkin DV, Berlin JM, Sinitskii A, Sun Z, Slesarev A, Alemany LB, Lu W, Tour JM (2010) Improved synthesis of graphene oxide. ACS Nano 4:4806–4814
27. Chen L, Xiao C, He X, Yu B, Kim SH, Qian L (2017) Friction and tribochemical wear behaviors of native oxide layer on silicon at nanoscale. Tribol Lett 65:1–8
28. Sader JE, Chon JW, Mulvaney P (1999) Calibration of rectangular atomic force microscope cantilevers. Rev Sci Instrum 70:3967–3969
29. Tang C, Jiang Y, Chen L, Sun J, Liu Y, Shi P, Aguilar-Hurtado JY, Rosenkranz A, Qian L (2023) Layer-dependent nanowear of graphene oxide. ACS Nano 17:2497–2505

30. Krishnamoorthy K, Veerapandian M, Yun K, Kim SJ (2013) The chemical and structural analysis of graphene oxide with different degrees of oxidation. Carbon 53:38–49
31. Yang D, Velamakanni A, Bozoklu G, Park S, Stoller M, Piner RD, Stankovich S, Jung I, Field DA, Ventrice CA, Ruoff RS (2009) Chemical analysis of graphene oxide films after heat and chemical treatments by X-Ray photoelectron and micro-raman spectroscopy. Carbon 47:145–152
32. Dave SH, Gong CC, Robertson AW, Warner JH, Grossman JC (2016) Chemistry and structure of graphene oxide via direct imaging. ACS Nano 10:7515–7522
33. Mkhoyan KA, Contryman AW, Silcox J, Stewart DA, Eda G, Mattevi C, Miller S, Chhowalla M (2009) Atomic and electronic structure of graphene-oxide. Nano Lett 9:1058–1063
34. Peng X-Y, Liu X-X, Diamond D, Lau KT (2011) Synthesis of electrochemically-reduced graphene oxide film with controllable size and thickness and its use in supercapacitor. Carbon 49:3488–3496
35. A YQ, B JL BYD, C XQFA, C QLA (2018) Impacts of environments on nanoscale wear behavior of graphene: edge passivation vs. substrate pinning. Carbon 139:59–66
36. Vasić B, Matković A, Ralević U, Belić M, Gajić R (2017) Nanoscale wear of graphene and wear protection by graphene. Carbon 120:137–144
37. Tang X, Lai KWC (2016) Substrate effect on atomic force microscopy-based nanolithography of graphene. IEEE Trans Nanotechnol 15:607–613
38. Qi Y, Liu J, Zhang J, Dong Y, Li Q (2017) Wear resistance limited by step edge failure: the rise and fall of graphene as an atomically thin lubricating material. ACS Appl Mater Interfaces 9:1099–1106
39. Chen L, Chen Z, Tang X, Yan W, Zhou Z, Qian L, Kim SH (2019) Friction at single-layer graphene step edges due to chemical and topographic interactions. Carbon 154:67–73
40. Li B, Cao X, Ong HG, Cheah JW, Zhou X, Yin Z, Li H, Wang J, Boey F, Huang W, Zhang H (2010) All-carbon electronic devices fabricated by directly grown single-walled carbon nanotubes on reduced graphene oxide electrodes. Adv Mater 22:3058–3061
41. Liu Y, Jiang Y, Sun J, Wang Y, Qian L, Kim SH, Chen L (2022) Inverse relationship between thickness and wear of fluorinated graphene:thinner is better. Nano Lett 22:6018–6025
42. Yu T, Shen R, Wu Z, Du C, Shen X, Jia N, Deng H, Zhao Y, Zhang L, Feng Y, Zhang Z, Luo Y, Zhou F, Wang D (2023) Monolayer $NbSe_2$ favors ultralow friction and super wear resistance. Nano Lett 23:1865–1871
43. Tran Khac B-C, Delrio FW, Chung K-H (2018) Interfacial strength and surface damage characteristics of atomically thin h-BN, MoS_2, and graphene. ACS Appl Mater Interfaces 10:9164–9177
44. Kwon S, Lee KE, Lee H, Koh SJ, Ko J-H, Kim Y-H, Kim SO, Park JY (2017) The effect of thickness and chemical reduction of graphene oxide on nanoscale friction. J Phys Chem B 122:543–547
45. Lee C, Li Q, Kalb W, Liu XZ, Berger H, Carpick RW, Hone J (2010) Frictional characteristics of atomically thin sheets. Science 328:76–80
46. Lee J, Novoselov KS, Shin HS (2011) Interaction between metal and graphene: dependence on the layer number of graphene. ACS Nano 5:608–612
47. Zhang M, Sun J, Mao Y, Liu G, Jin W (2019) Effect of substrate on formation and nanofiltration performance of graphene oxide membranes. J Membr Sci 574:196–204
48. Chen C-M, Huang J-Q, Zhang Q, Gong W-Z, Yang Q-H, Wang M-Z, Yang Y-G (2012) Annealing a graphene oxide film to produce a free standing high conductive graphene film. Carbon 50:659–667
49. Liu J, Lin Z, Liu T, Yin Z, Zhou X, Chen S, Xie L, Boey F, Zhang H, Huang W (2010) Multilayer stacked low-temperature-reduced graphene oxide films: preparation, characterization, and application in polymer memory devices. Small 6:1536–1542
50. Shin H-J, Kim KK, Benayad A, Yoon S-M, Park HK, Jung I-S, Jin MH, Jeong H-K, Kim JM, Choi J-Y, Lee YH (2009) Efficient reduction of graphite oxide by sodium borohydride and its effect on electrical conductance. Adv Funct Mater 19:1987–1992
51. Pei S, Zhao J, Du J, Ren W, Cheng HM (2010) Direct reduction of graphene oxide films into highly conductive and flexible graphene films by hydrohalic acids. Carbon 48:4466–4474
52. Akhavan O (2010) The effect of heat treatment on formation of graphene thin films from graphene oxide nanosheets. Carbon 48:509–519
53. Huh SH (2011) Thermal reduction of graphene oxide. Phys Appl Graphene Exp 19:73–90
54. Sengupta I, Chakraborty S, Talukdar M, Pal SK, Chakraborty S (2018) Thermal reduction of graphene oxide: how temperature influences purity. J Mater Res 33:4113–4122
55. Becerril HA, Mao J, Liu Z, Stoltenberg RM, Bao Z, Chen Y (2008) Evaluation of solution-processed reduced graphene oxide films as transparent conductors. ACS Nano 2:463–470

Publisher's Note Springer Nature remains neutral with regard to jurisdictional claims in published maps and institutional affiliations.

Chuan Tang is currently a Ph.D. candidate in mechanical engineering at Southwest Jiaotong University, Chengdu, China. His research interest mainly involves nanowear and nanofabrication.

Lei Chen is currently a professor of Southwest Jiaotong University (SWJTU), Chengdu, China. He received his Ph.D. degree from SWJTU in 2013 and acted as a visiting scholar in The Pennsylvania State University, USA. His current research interests involve micro/nano-tribology and atomic level manufacturing. He is the author and co-author of 87 original research papers. He is in charge of more than 20 projects, including NSFC-outstanding youth foundation (2021). He is the editorial or youth editorial board member of the 6 journals, including Chinese Journal of Mechanical Engineering, Nanomanufacturing and Metrology and so on.

Linmao Qian currently a professor of mechanical engineering at Southwest Jiaotong University (SWJTU), Chengdu, China. He received his B.S. (1994) and Ph.D. (2000) degree in mechanical engineering from Tsinghua University in China. After two years at Ecole Normale Supérieure in Paris and one year at the Hong Kong University of Science and Technology as a postdoctoral researcher, he joined the SWJTU in 2002. His research interests include nanotribology and atomic level manufacturing. He has published more than 360 peer-reviewed journal papers and authorized more than 30 patents. He is the co-editor of Jurnal Tribologi, associate editor of Chinese Journal of Mechanical Engineering, and a member of editorial board of eight journals, such as Friction and the Proceedings of the Institution of Mechanical Engineers, Part J: Journal of Engineering Tribology.

Authors and Affiliations

Chuan Tang[1] · **Lei Chen**[1] · **Linmao Qian**[1]

✉ Lei Chen
chenlei@swjtu.edu.cn

Chuan Tang
chuan2018@my.swjtu.edu.cn

Linmao Qian
linmao@swjtu.edu.cn

[1] Tribology Research Institute, The State Key Laboratory of Rail Vehicle System, School of Mechanical Engineering, Southwest Jiaotong University, Chengdu 610031, China